doi:10.26443/seismica.v5i2.2809

Seismotectonics of the Mount St. Helens Region

Brenton W. Hirao * [1,4], **Amanda M. Thomas** [1], **Weston A. Thelen** [2], **David R. Shelly** [3], **Cyril Journeau** [1], **Alexandra M. Iezzi** [2]

[1]Department of Earth Sciences, University of California, Davis, California, United States, [2]U.S. Geological Survey, Cascades Volcano Observatory, Vancouver, Washington, United States, [3]U.S. Geological Survey, Earthquake Hazards Science Center, Golden, Colorado, United States, [4]Department of Earth Sciences, University of Oregon, Eugene, Oregon, United States

Author contributions: *Conceptualization*: B. Hirao, A. Thomas, W. Thelen. *Data Curation*: B. Hirao, A. Thomas, W. Thelen, D. Shelly. *Formal Analysis*: B. Hirao, A. Thomas, W. Thelen. *Funding Acquisition*: A. Thomas. *Investigation*: B. Hirao, A. Thomas, W. Thelen. *Methodology*: B. Hirao, A. Thomas, D. Shelly. *Project Administration*: A. Thomas, W. Thelen. *Resources*: A. Thomas. *Software*: B. Hirao, D. Shelly. *Supervision*: A. Thomas. *Validation*: B. Hirao, A. Thomas, W. Thelen, D. Shelly, C. Journeau, A. Iezzi. *Visualization*: B. Hirao, W. Thelen. *Writing – Original draft*: B. Hirao, A. Thomas, W. Thelen, D. Shelly, C. Journeau, A. Iezzi. *Writing – Review and editing*: B. Hirao, A. Thomas, W. Thelen, D. Shelly, C. Journeau, A. Iezzi.

Abstract The St. Helens seismic zone is a dextral fault zone in the Cascade Arc upper crust that underlies the Mount St. Helens volcanic complex, in which two earthquakes of magnitude 5 or greater have been recorded since 1960. To improve our understanding of fault structures around Mount St. Helens, we apply a high-precision template-matching and location procedure to create two enhanced seismicity catalogs: a long-term catalog spanning the 2008 to 2024 study period, and a short-term catalog that leverages a dense network of temporary seismometers between July 2014 and July 2016. We make further use of the temporary network to resolve 181 well-constrained fault-plane solutions. Inspection of the two seismicity catalogs shows that seismicity is persistent within four distinct groups that surround the Mount St. Helens volcano—these groups do not interact with each other, nor with volcano-tectonic seismicity. Moreover, fault plane solutions from these four groups suggest that Mount St. Helens may be underlain by two sub-orthogonal fracture zones. We propose that the intersection of these two fracture zones forms a high permeability pathway for mantle-wedge-sourced volatiles to ascend towards the surface from lower to midcrustal depths, thus aiding in the development of the modern-day Mount St. Helens magmatic transport system.

Production Editor: Gareth Funning
Handling Editor: Christos Evangelidis
Copy & Layout Editor: Théa Ragon

Received: Mars 9, 2026
Accepted: November 3, 2026
Published: November 19, 2026

Non-technical summary The Mount St. Helens volcano is positioned above the St. Helens seismic zone, a major crustal fault in southern Washington, United States that has generated two earthquakes of magnitude 5 or greater between 1960 and the present day. To better understand this fault, we create high resolution earthquake catalogs spanning between 2008 and 2024. We also analyzed data from a dense network of seismometers temporarily installed around the volcano between 2014 and 2016. Our results reveal four distinct groups of earthquakes surrounding Mount St. Helens. These groups have remained active over the 2008 to 2024 study period and appear to behave independently of one another and of earthquakes associated with volcanic activity. By examining how these faults move during earthquakes, we find evidence for two intersecting zones of fractures beneath the volcano. We suggest that these intersecting fractures may provide pathways for hot fluids and gases from deep within the Earth to rise toward the surface, potentially helping establish the underground system that transports magma toward Mount St. Helens.

1 Introduction

Seismicity adjacent to volcanic systems can be attributed to the superposition of stresses imposed by the magmatic transport system, local geologic heterogeneities, and the regional-scale tectonic stress field. The St. Helens seismic zone (Fig. 1) is a right-lateral NNW–SSE oriented strike-slip crustal shear zone that underlies the modern-day Mount St. Helens volcanic complex (Grant et al., 1984; Weaver et al., 1987; Qamar et al., 1987). The St. Helens seismic zone was initially characterized using fault-plane solutions of events from as early the September 1961 M5.1 event near Swift Reservoir and February 1981 M5.5 sequence near Elk Lake, Washington (Fig. 1; Weaver and Smith, 1983; Grant et al., 1984; Weaver et al., 1987). Both historical examples show that the St. Helens seismic zone can generate potentially damaging earthquakes of a moderate magnitude. To our knowledge, displacement rates along the St. Helens seismic zone at the surface are too low to be resolved through modern Global Navigation Satellite System (GNSS) monitoring. Moreover, there are no known geomorphic expressions due to displacement along the St. Helens seismic zone. Thus, the St. Helens seismic zone remains characterized primarily through seismic studies—including earthquake locations, fault-plane solutions (Grant et al., 1984; Weaver et al., 1987; Qamar et al., 1987), tomographic imaging (Waite and Moran, 2009; Bedrosian et al., 2018; Kiser et al., 2019; Ulberg et al., 2020), and geothermal surveys (Norman et al., 2015; Steely et al., 2021).

*Corresponding author: bhirao@ucdavis.edu

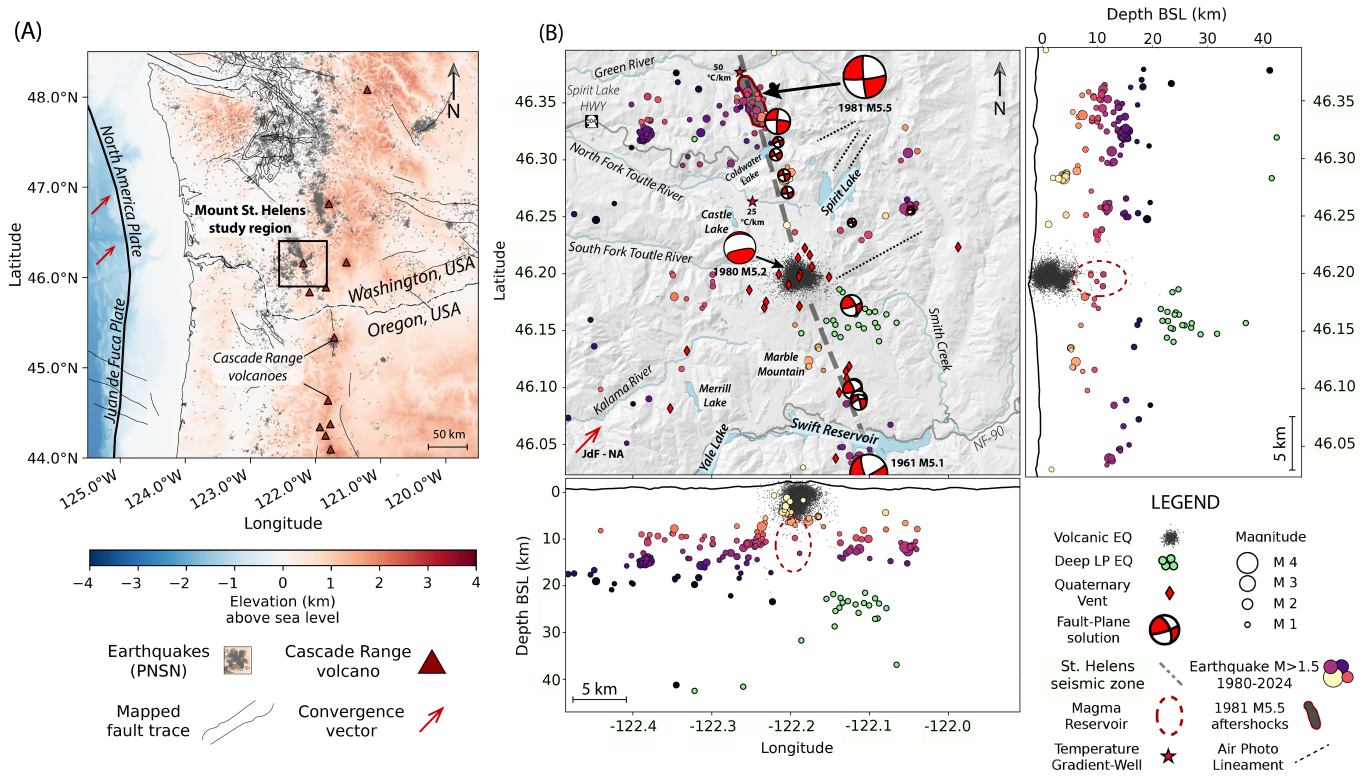


Figure 1 Pacific Northwest region (A) and Mount St. Helens study area (B). (A) shows select earthquakes from the PNSN catalog and Juan de Fuca-North American plate boundary. Juan de Fuca and North American convergence vector is sourced from the ITRF2020 model (Altamimi et al., 2023). Locations of the Cascade volcanoes are from the Smithsonian active volcanoes catalog. Mapped fault traces are from the USGS Quaternary faults database. (B) shows seismicity from the PNSN catalog with magnitude greater than M1.5, volcanic earthquakes (EQ) from Hirao et al. (2025), Deep Long Period (LP) events from the PNSN catalog, Quaternary volcanic vents from O'Hara et al. (2020), historical fault-plane solutions from 1961-1985 and the Saint Helens Seismic Zone trace from Weaver and Smith (1983), and approximate upper-crustal magma reservoir location from Kiser et al. (2016) Moment tensor for the 1980 M5.2 represents the Mount St. Helens eruption of May 1980 and is sourced from the Global Centroid Moment Tensor project (Dziewonski et al., 1981; Ekström et al., 2012). Temperature gradient well data from Norman et al. (2015) Air Photo Lineaments reflect pyrite-bearing dikes and are simplified from Evarts et al. (1987)

The St. Helens seismic zone may partially contribute to the location of the modern-day edifice of Mount St. Helens. Mount St. Helens is unique from other Cascade Range volcanoes in southern Washington and northern Oregon for its high background earthquake activity rates (e.g., Moran, 1994; Zhang et al., 2022; Hirao et al., 2025), and for its anomalously large westward offset from the main volcanic axis (Fig. 1A, e.g., Hildreth, 2007; Hansen et al., 2016; Bedrosian et al., 2018). Moreover, unlike other Cascade Range volcanoes, Mount St. Helens is geographically surrounded by nonvolcanic earthquakes (Fig. 1A). Magnetotelluric and seismic imaging of central and southern Washington indicate that the St. Helens seismic zone at midcrustal depths forms a lithologic boundary that separates the Siletzia oceanic basalts and Spirit Lake batholith granodiorites to the west and east, respectively (Finn and Williams, 1987; Hill et al., 2009; Bedrosian et al., 2018; Kiser et al., 2019; Ulberg et al., 2020). In addition, observations of low P-wave velocity (Vp) anomalies, high conductivity, persistent deep long-period event activity (Nichols et al., 2011; Han et al., 2018), and elevated fluid geothermal observations taken at Green River (Fig. 1B; Norman et al., 2015) suggest that the St. Helens seismic zone may serve to channel melt and volatiles from lower and midcrustal depths towards the surface (Hill et al., 2009; Bedrosian et al., 2018). A slight change of strike of the St. Helens seismic zone is thought to form a small pull-apart extension beneath Mount St. Helens volcano, allowing for decompression melting and the upward movement of melt towards shallow depths (Weaver et al., 1987).

Earthquake locations, timing, and their associated fault-plane solutions can be helpful to characterize deformation along active structures. To understand the potential for interaction between fault and magmatic systems, we generate two enhanced seismicity catalogs—both consisting of earthquakes surrounding the volcano. The first catalog spans from January 1, 2008 to December 31, 2023, and consists of earthquakes recorded on a total of 59 permanent broadband seismometers within roughly 50 km of Mount St. Helens. The second catalog, which we refer to as the 'XD' or Imaging Under Mount St. Helens (iMUSH) catalog, is shorter in duration, spans from July 2014 to July 2016 and consists of earthquakes that are recorded on the permanent UW, CC, UO, and PB networks in addition to 65 temporary nodal seismometers included in the

iMUSH dense-array experiment (Creager, 2014; Kiser et al., 2016). Compared with the longer catalog, the iMUSH catalog contains fewer events in total; however, the dense network configuration of iMUSH stations allows for the detection, location, and characterization of larger quantities of small-magnitude earthquakes during the 2014 to 2016 period. In addition, the good azimuthal coverage configuration of the iMUSH network is well suited to detecting earthquakes—which we leverage to solve for focal mechanisms to improve the characterization of the St. Helens seismic zone and adjacent faults.

2 Methods

2.1 Event detection and location

To generate both earthquake catalogs, we apply the shift-and-stack template-matching detection and location procedure described in Hirao et al. (2025), which is similar to the approach of Shelly et al. (2016) and briefly summarized here. We generate individual P- and S-wave waveform templates from 3,133 analyst-verified earthquakes from the event catalog distributed by the Pacific Northwest Seismic Network (PNSN, University of Washington, 1963). We select events that locate at least 1 km away from the edge of the velocity model study area (see Hirao et al., 2025), have at least 4 stations, and have a maximum azimuthal gap of 300 degrees. Each waveform template is 2.5 seconds in duration and begins 0.5 seconds before its respective phase arrival time. For stations that do not have S-wave arrivals, we predict the S-wave arrival using a Vp/Vs ratio of 1.73. If the S-P arrival times are less than 2.5 seconds, we truncate the P-wave arrival to exclude the S-wave. To assign template event starting locations, we apply the NonLinLoc OCT-TREE grid search (Lomax et al., 2001, 2009) to find optimal location solutions (Fig. S1) within 3-dimensional (3D) P- and S-wave travel time grids derived from the 3D velocity models of Kiser et al. (2019). Prior to cross-correlation, we load, detrend, interpolate to 100 samples per second, and apply a two-way bandpass Butterworth filter with 2 and 20 Hz corner frequencies using the Obspy software (Beyreuther et al., 2010). We then cross-correlate each waveform template through the processed day-long waveforms streams and evaluate 100 Hz normalized cross-correlation (NCC) functions with the Super-Efficient Cross Correlation package of Senobari et al. (2018). Both templates and continuous day-long waveforms are detrended and filtered in the same way. We consider event detections where summed peak values of the summed NCC value exceed 12 times its median absolute deviation (MAD) for that day. Cross-correlation peak values and timing for individual traces and phases within 0.5 second of the shifted differential times are stored if they exceed 8 times their respective MAD. The resulting differential times and NCC values are then input into the GrowClust3D algorithm (Trugman et al., 2023) for relative relocation using the same 3D travel-time grids used for absolute starting locations. Lastly, we remove all events that locate at the edge of the velocity model space.

2.2 Long-term catalog construction

To construct the long-term catalog for the 2008 to 2024 study period (spanning January 1, 2008 to December 31, 2023; Figs. 2A, 3), we apply the template matching procedure to stations of the regional network—including a total of 59 broadband seismometers in the University of Washington (UW; University of Washington, 1963), Cascade Chain (CC; Cascades Volcano Observatory/USGS, 2001), Plate Boundary Observatory (PB; UNAVCO), and University of Oregon (UO; University of Oregon, 1990) networks within the 100- by 90-km region around Mount St. Helens. We construct P- and S-waveform templates from 3,171 analyst-picked and verified events contained in the PNSN catalog, recorded from January 2008 to December 2023 (Fig. S1). All templates and new detections analyzed in this catalog are at least 4 km away from the center of Mount St. Helens.

2.3 Methods for short-term (iMUSH) catalog

To construct the short-term iMUSH catalog (Figs. 2B, 3), we apply the template-matching and location procedure described above to a total of 65 stations from the iMUSH dense-array experiment, in addition to all stations from the permanent network that recorded from July 2014 to August 2016 (XD network; Creager, 2014). The iMUSH dense-array experiment is a temporary geophone and seismometer network (network code XD) that continuously recorded ground motion in the region surrounding Mount St. Helens region between July 2014 and August 2016 (e.g., Kiser et al., 2016). Although originally designed to produce high-resolution tomographic models of the Mount St. Helens volcanic complex after its latest eruption (ending in 2008; e.g., Dzurisin et al., 2015; Dzurisin, 2018), its dense and widespread configuration is also favorable for capturing microseismicity distal to the Mount St. Helens edifice where permanent network coverage is sparse (especially east and south of Mount St. Helens; Fig. 2). Here, the detection and location procedures are performed separately from the long-term catalog.

Similar to the long-term catalog, we construct separate waveform templates from P- and S-waveform arrivals of 540 PNSN catalogued events recorded from July 2014 to August 2016. Each event template includes analyst-verified phase picks from the PNSN on permanent network stations in addition to arrivals recorded on the XD network. Since the PNSN does not use the XD network to monitor seismicity, P- and S-wave phase arrivals on XD network stations are not included in the 2014–2016 event templates. Thus, we add to the 2014–2016 event templates P- and S-wave phase arrivals generated by a combination of manual and automated phase picking with the PhaseNet convolutional neural network (Ronneberger et al., 2015; Zhu and Beroza, 2019). To reduce the workload of phase-picking, we apply the PhaseNet algorithm with model weights trained on the Stanford Earthquake Database (Mousavi et al., 2019) included in the Seisbench package (Woollam et al., 2022) to a 60 second window beginning at the PNSN catalog event origin time to all XD stations within a 50 km radius of its epicenter.

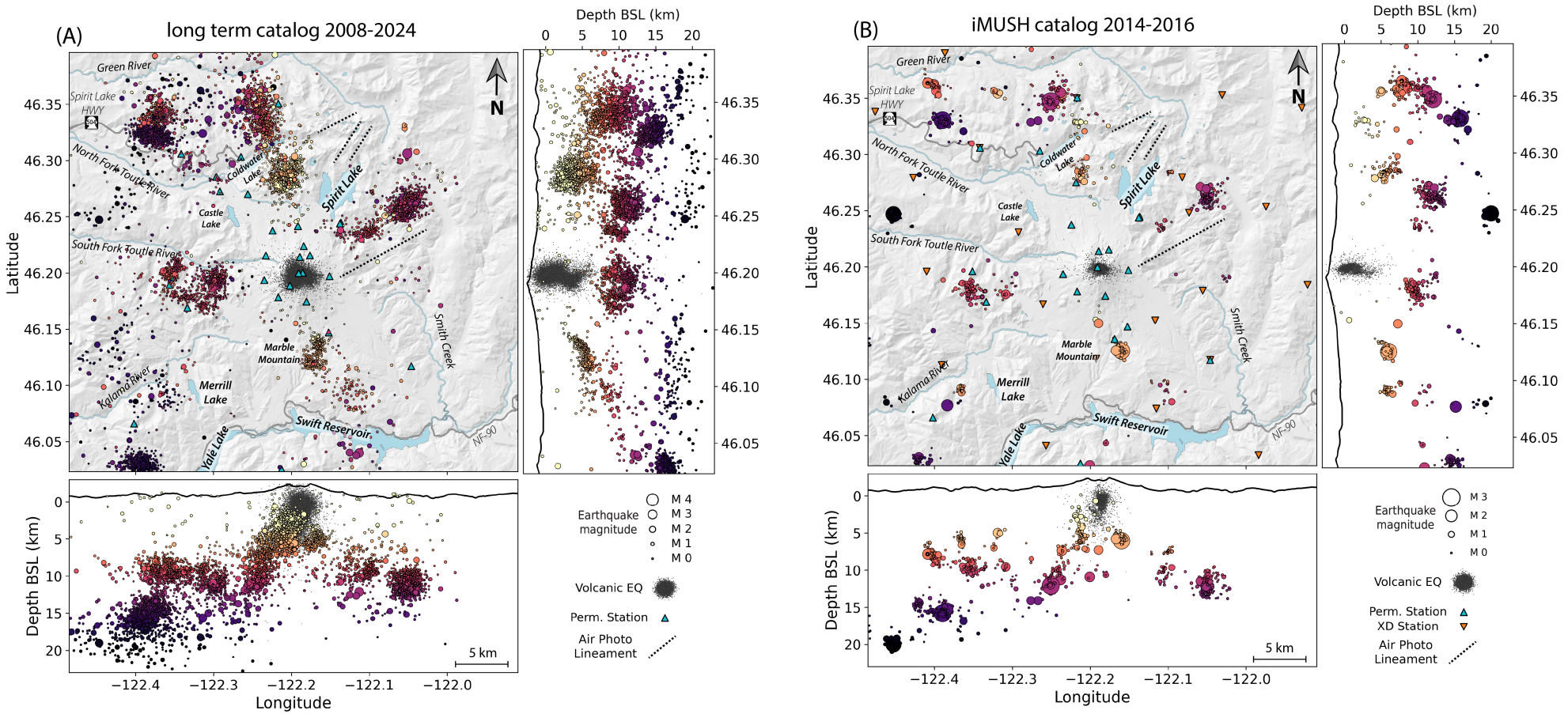


Figure 2 Locations of events in the long-term catalog from 2008 to 2024 in Panel (A), and 2014–2016 catalog from the Imaging Under Mount St. Helens (iMUSH) dense array experiment (network code XD) in (B). For the sake of visibility, the earthquake magnitude marker scales are different in both panels. (B) only shows permanent stations that were active during the 2014–2016 period. The colored dots are the nonvolcanic events analyzed in this study—they are colored according to depth in km below sea level (BSL) (see Depth/Longitude and Depth/Latitude sections). Air Photo Lineaments reflect pyrite-bearing dikes and are simplified from Evarts et al. (1987). Volcanic earthquakes (EQ) are dark grey and unscaled—these are analyzed in depth in Hirao et al. (2025).

We save all P- and S-wave phase arrival picks with a minimum confidence of 0.3. We then manually inspect the arrivals of each event, discard mistimed and misclassified arrivals, and manually impute additional missing arrivals using the Snuffler graphical user interface included in the Pyrocko distribution (Heimann et al., 2017). We use these phase picks to solve for the starting locations of templates with the NonLinLoc package and 3D velocity models (Kiser et al., 2019). Like the construction of the long-term catalog, new event solutions are resolved using the GrowClust3D relative location procedure.

2.4 Event magnitudes

To quantify the size of newly detected earthquakes, we extend the local Richter magnitudes (M_L) included in the PNSN catalog to new detections by applying the relative amplitude scaling procedure of Shelly et al. (2016) (Equation 1).

$$M_{new} = M_{template} + c * \log_{10} \alpha \quad (1)$$

Here, α represents the amplitude ratio between a given template and the new event waveform, and c is a scaling constant that maps the measured amplitude ratio (α) to a magnitude differential (M_L). To determine the c value, we compute the amplitude ratio for each catalog template pairwise against their respective catalog M_L difference. We then empirically determine a value of $c = 0.57$ using the Huber robust linear least squares algorithm included in the SciKit Learn package (Fig. 4A; Pedregosa et al., 2011). Values of is α are computed at maximum waveform alignment, through an eigenvector decomposition of the covariance matrix of the template and new event waveforms. Although local magnitudes (M_L) of new events can be estimated directly from equivalent Wood–Anderson peak displacements (e.g., Richter, 1935; Hutton and Boore, 1987), we favor extending network catalog magnitudes to automatically detected and located events using relative amplitudes. This approach avoids removal of instrument-response and simulation of a Wood–Anderson instrument while maintaining consistency with the PNSN magnitude scale through calibration with analyst-reviewed magnitudes.

We favor the M_L values as starting magnitudes for two reasons: over half of the templates (1,752 of 3,171) are assigned M_L values, and unlike the supplied coda duration magnitudes (M_d), M_L does not rely on coda durations, which can vary significantly due to individual site effects. For the remaining 1,419 event templates that are assigned M_d values and are without M_L, we estimate the equivalent M_L using a linear scaling relationship derived from a total of 1,249 events that have both M_d and M_L values (Equation 2; Fig. S1).

$$M_L = 0.82 * M_d + 0.25 \quad (2)$$

2.5 Fault-plane solutions

Fault plane solutions (FPS, a.k.a. focal mechanisms) are a convenient way to represent the orientation of slip along a fault surface during an earthquake with an assumed double-couple point source (e.g., Aki and Richards, 1980; Vavryčuk, 2015). We make further use of the station coverage offered by the XD network to resolve fault-plane solutions for PNSN catalogued events recorded from 2014 to 2016. We manually assign polarity values between -1 (negative) and 1 (positive) through visual inspection of all P-wave arrivals from the PhaseNet algorithm on vertical channels. Each polarity is a value between -1 (dilatation, down) and 1 (compression, up) and is weighted by a factor between 0 and 1 to reflect the subjective measurement confidence. We also include the first motion polarities assigned by the PNSN analysts on permanent network stations (IRIS Data Management Center; Trabant et al., 2012; University of Washington, 1963), which are either 1 or -1 for compression and dilatation, respectively.

To further aid in constraining FPSs, we include S/P amplitude ratios for stations that include a P-wave arrival time (Hardebeck and Shearer, 2002). If an S-wave arrival pick is not present, we crudely predict the S-wave arrival with an S to P travel-time ratio of 1.73. The peak-to-peak amplitude for each phase is then computed as the maximum value minus the minimum value of the waveform for a 2.5 second window, beginning at 1 second before its respective arrival time pick. If the S-P time is less than 2.5 seconds, we make sure to exclude the S-wave arrival from the waveform. We take the S/P amplitude ratio as the ratio of these two values for S and P phases and assume that the noise levels prior to both arrival times are the same. We do not apply station corrections to the amplitudes. Next, we estimate ray-path take-off angles and azimuths for polarity and amplitude ratio observations using the NonLinLoc Time2EQ program (Lomax et al., 2001, 2009) as well as 3D P-wave travel time grids and event locations from GrowClust3D. We require that each event be associated with a minimum of 8 polarity observations and a maximum azimuthal gap of 90 degrees and assume that 10% of both polarity and S/P amplitude ratio observations are incorrect. Lastly, we input into SKHASH (Skoumal et al., 2024) a list of polarity reversals reported by the PNSN to account for stations with inverted vertical channel orientations. The first motion polarities and S/P amplitude ratios are then jointly inverted for the optimal FPS using the method of Skoumal et al. (2024). Here, we report the FPS for a total of 181 events recorded from 2014 to 2016 (Fig. 5). To be selected for the result, we require a maximum nodal plane uncertainty of 25 degrees and a quality score of 'A' or 'B' (see manual of Skoumal et al., 2024).

2.6 Permanent-network moment tensors

For discussion, we include from the PNSN catalog the moment tensor solutions for two of the largest earthquakes recorded within the study period: a M_d 4.3 (M_w 3.84) event on February 14, 2011 (event id: uw10816153) and M_L 3.9 (M_w 3.76) event on January 3, 2018 (event id: uw61362346) (Fig. 3). The M_d 4.3 event is located roughly 7 km NNW of Mount St. Helens at a depth of 4 km below sea level (BSL). This event is fit by

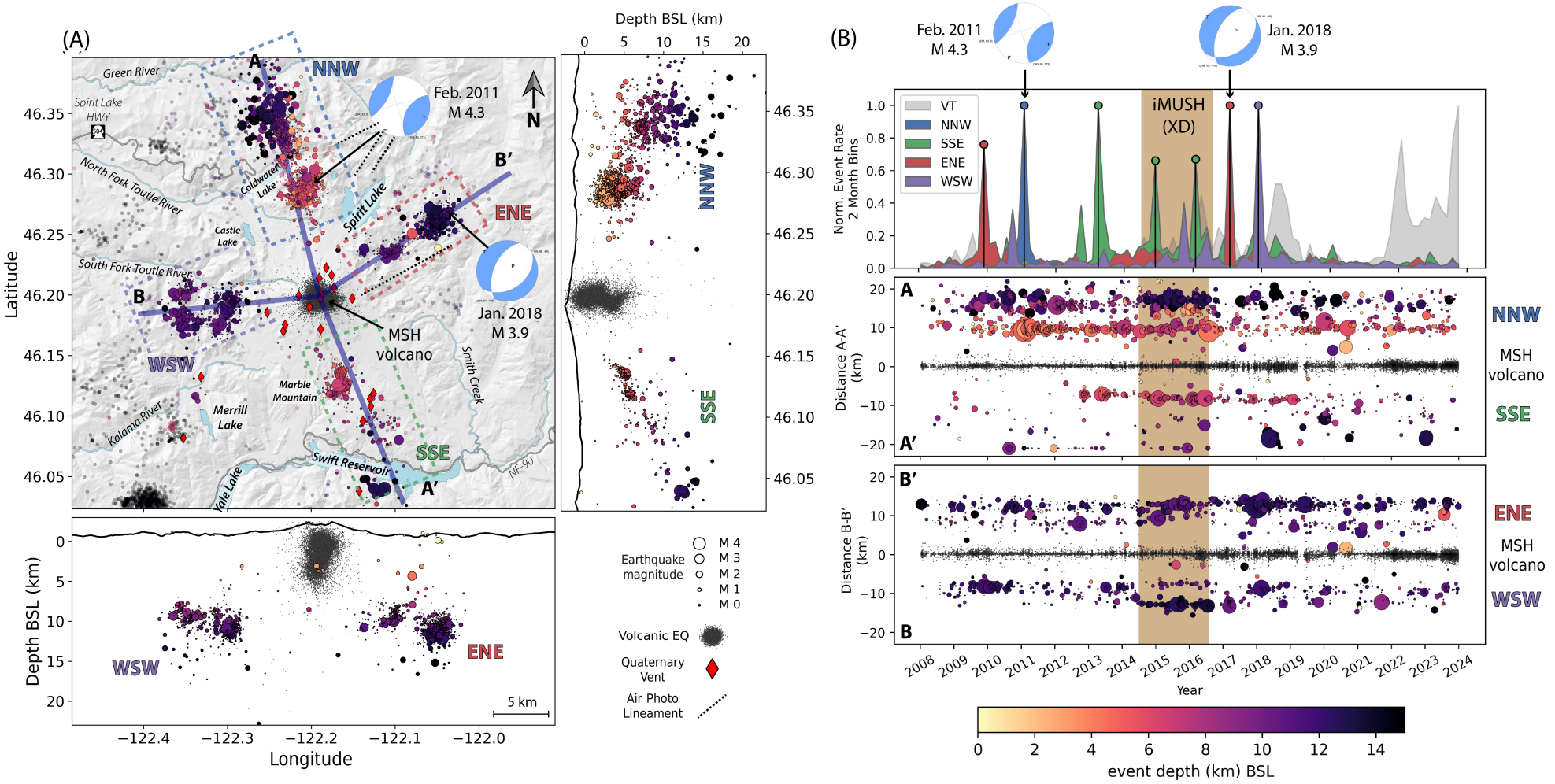


Figure 3 Figure 3: The four seismicity groups from 2008 to 2024. Seismicity from 2008 to July 2014 and August 2016 to 2024 is from the long-term catalog. Events from July 2014 to August 2016 are from the Imaging Under Mount St. Helens (iMUSH) catalog. Volcano-tectonic earthquakes (VT or Volcanic EQ) from Mount St. Helens (MSH) are from Hirao et al. (2025) and are unscaled. In panel (A), the A-A' and B-B' profiles are used to analyze spatial distributions of all four non-volcanic seismicity groups, shown in panel (B). Event depths are shown in km below sea level (BSL). The beachballs of moment tensor solutions of two of the largest events are from the Pacific Northwest Seismic Network catalog from the 2008 to 2024 study period. Cross sections depict events within the WSW–ENE and SSE–NNW seismicity groups. Events not contained in the four groups are transparent dots. Panel (B) shows normalized (Norm.) event rates in 2 month-long bins for all four seismicity groups in addition to VT seismicity from Hirao et al. (2025), along-profile distances for the NNW and SSE groups along the A-A' profile and WSW and ENE groups along B-B' profile. The events in both A-A' and B-B' profiles are either VT events (grey, unscaled) from Hirao et al. (2025) or those contained within the dashed lines in (A) for the NNW–SSE and WSW–ENE groups, respectively. The colorbar applies to the depths for both panels (A) and (B). Air Photo lineaments reflect pyrite-bearing dikes and are simplified from Evarts et al. (1987)

a 33% double-couple component and steeply dipping NNW–SSE (strike, dip, and rake of 254/83/5 degrees) and ENE–WSW (strike, dip, and rake of 163/85/173 degrees) oriented nodal planes. The M_L 3.9 event is located roughly 10 km ENE of Mount St. Helens and 10 km depth BSL. It is fit completely by a double-couple mechanism, NNE–SSW oriented normal-faulting auxiliary planes (strike of 55 degrees azimuth and dip of 40 degrees). Because moment tensor solutions are sensitive to location parameters, we assume the location provided by the U.S. Geological Survey catalog when discussing the two events. After relocation with the 3D velocity models, NonLinLoc, and GrowClust3D procedures, both events retain similar location solutions as their respective PNSN solutions. The February 2011 event (uw10816153) relocation is shallower than the PNSN solution by 380 meters with negligible horizontal change. The January 2018 event (uw61362346) shifts by 528 meters horizontally and is 1.55 km deeper than the PNSN solution.

3 Results

Between 2008 and 2024 we record a total of 10,331 earthquakes (approximately 3 times greater than in the PNSN catalog) within a region approximately 5 to 50 km of the Mount St. Helens volcanic edifice, with the majority of the seismicity located between 5 to 30 km from the modern-day edifice of Mount St. Helens (Fig. 2, Fig. 3). There is a distinct gap that separates the volcanic seismicity from the surrounding seismicity (Fig. 2). Earthquakes directly beneath the volcanic edifice between 2008 to 2024 are analyzed in Hirao et al. (2025) and are only considered for reference in this study (Fig. 1, 2, 3). Approximately 65% (6,696 of the 10,331) of all observed events adjacent to the Mount St. Helens volcano are organized into four geographically distinct groups that are positioned to the NNW, SSE, WSW, and ENE of the edifice (Fig. 2, 3).

3.1 Four nonvolcanic earthquake groups

For spatial and temporal analysis, we isolate and refer to these four groups of earthquakes according to their position relative to Mount St. Helens at a latitude and longitude of 46.19 and -122.19 degrees and consider the rest as a part of the geographic 'background' (Figs. 2, 3). In addition, we treat the NNW—SSE and WSW—ENE groups as opposing pairs with respect to the middle of Mount St. Helens for additional spatial analysis. Here we seek to compare the relative positions of each group in both pairs not only with respect to each other, but in addition to Mount St. Helens. To do so, we project the distance of the two pairs along two curvilinear profiles: A-A' and B-B', respectively (Fig. 3). Both profiles are defined by three points and intersect at the middle of Mount St. Helens, which we treat as the origin.

In addition, we define a magnitude of 'completeness' (M_c) to describe the lowest event magnitude that is completely detected by our methods, according to the Gutenberg-Richter scaling law (e.g., Utsu, 1999). For each catalog and each seismicity group, we bin all event magnitudes into 0.1 magnitude bins, then assume that M_c is the magnitude bin with the highest count (i.e. the 'peak' of the magnitude distribution). We consider this simple M_c adequate for comparing detection thresholds between network geometries used to construct each catalog.

The geographic footprint of the NNW and SSE seismicity groups is consistent with the orientation and extent of the St. Helens seismic zone (Fig. 1), previously defined by Weaver et al. (1987). The NNW seismicity group is spatially the largest (between 5.5 and 28 km NNW of Mount St. Helens) and most populous of all four and contains a total of 2,952 events within a continuous, NNW-oriented quasi-linear feature. The southernmost extent is near the head of the North Fork Toutle River at the Pumice Plain, extends NNW beneath Coldwater Lake, and reaches its northernmost extent at the Green River. The SSE group contains a total of 794 events (about 3.7 times fewer than in the NNW) and spans from its northernmost end at about 5 km south of Mount St. Helens and forms a trend that deviates from the NNW group towards the southeast direction. Here, it extends beneath a series of Quaternary volcanic vents (O'Hara et al., 2020) southwards toward the eastern end of Swift Reservoir. The SSE group is less spatially continuous than the NNW group, likely owing to its smaller event count. While earthquakes within the NNW group occupy a greater range of depths than in the SSE group, they share similar median depths of 4.2 and 5.3 km BSL, respectively. Event depths within the NNW and SSE groups are shallowest at roughly 3–6 km BSL near the volcano and appear to increase up to 5–15 km BSL away from the volcano (Figs. 3A, S4). For these events, depth uncertainties from both the relative and absolute location solutions show a small positive correlation with distance from the volcano (Fig. S4). However, most event depth uncertainties are well within the change in event depth away from the volcano.

The WSW and ENE seismicity groups are positioned roughly opposite each other on either side of Mount St. Helens, and each is separated from seismicity directly beneath the edifice by approximately 5 km (Figs. 2, 3). The WSW group is bounded to the north and south between the South Fork Toutle River and Kalama River, respectively, between 5 to 15 km west of Mount St. Helens. The ENE group is separate from earthquakes within the edifice by a similar distance and forms an ENE-striking lineation southeast of Spirit Lake that extends from 5 to 18 km away from the volcano. The WSW and ENE groups each occupy similar depth ranges between 7 to 13 km BSL with median depths of 10.3 and 11.3 km, respectively. We detect and locate a total of 1,966 earthquakes within the ENE group, about twice as many as in the WSW group. Unlike events from the NNW and SSE groups along the St. Helens seismic zone, we do not observe a systematic variation in depth with respect to distance from the volcano.

All four seismicity groups feature persistent activity within the 2008 to 2024 study period (Fig. 3B). Normalized binned seismicity rates for all four groups are shown in Fig. 3B. Here, we compare seismicity rates among the four groups by binning the event counts

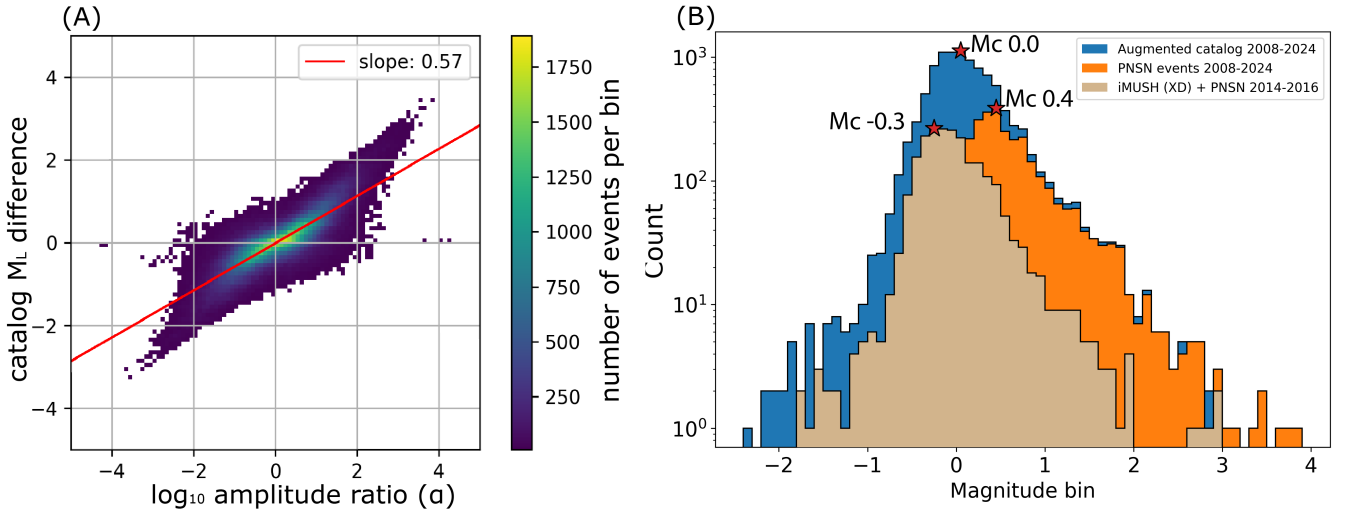


Figure 4 Relative magnitude calibration in panel (A) and magnitude distributions in panel (B). In panel (A), we calibrate the relative magnitude c coefficient by scaling the pairwise difference in the catalog local Richter magnitude (M_L) against the $\log_{10}$ of the amplitude ratio. See Section 2.4 for details. We adopt a solution of $c = 0.57$ to solve for relative magnitudes. Panel (B) shows magnitude-frequency distributions for the Pacific Northwest Seismic Network (PNSN) catalog 2008–2024, the long-term augmented catalog 2008 to 2024, and the Imaging Under Mount St. Helens (iMUSH) XD augmented catalog 2014–2016. The magnitude of completeness (M_c) for each distribution is assumed as the peak magnitude bin according to the Maximum Curvature definition of Wiemer and Wyss (2000)

in each group into non-overlapping two-month intervals. We then normalize each time-series with respect to their own maximum rates. For reference, we include the seismicity rates of volcano-tectonic (VT) events from Mount St. Helens. Peak activity rates for all groups occur from 2009 to 2018. Unsurprisingly, local peak seismicity rates within each of the four seismicity groups are temporally correlated to their largest magnitude events.

The largest event recorded in this study period is a M_L 4.3 in the NNW group between Spirit Lake and Coldwater Lake on February 14, 2011. The second highest magnitude event, also the largest event in the ENE group, is a M_L 3.9 ESE of Spirit Lake on January 3, 2018. Both earthquakes have been assigned moment tensor origin products by the PNSN. The largest magnitude earthquake of the SSE and WSW groups are a M_L 2.9 near Marble Mountain on February 8, 2016, and a M_L 2.2 near the South Fork Toutle River on July 9, 2013, respectively.

We do not find any clear correlation for elevated seismicity rates between the four groups, nor from within the volcano during the 2008 to 2024 study period. In addition, seismicity within the respective groups does not appear to migrate to any other group, or in/out of Mount St. Helens. Thus, there is no clear evidence for triggering or interaction among seismicity groups or the volcanic system.

The amplified detection capacity owing to the inclusion of 65 stations from the temporary XD network permits us to detect and locate a total of 2,236 events between July 1, 2014 and July 31, 2016, roughly 1.6 times greater than the long-term catalog in the same period. The improved station coverage enables detection and location of a greater number of small magnitude earthquakes, which is made apparent by a M_c of -0.3 in the iMUSH catalog, as opposed to 0.0 in the long-term catalog (Fig. 4B). In addition, the improved network allows for earthquakes to be more precisely located across the entire study region. The distributions of median absolute deviation uncertainties for all four seismicity groups are shown in Figure S2. Median horizontal and depth errors for the long-term catalog range from 0.4 km to 0.7 km and 0.4 to 0.8 km, respectively. By comparison, the median horizontal and depth uncertainties for events in the iMUSH catalog for those same groups range from 0.1 to 0.3 km and 0.1 to 0.5 km, two to five times smaller than in the long-term catalog. The increase of event depths with distance from the volcano in the NNW and SSE groups we observe in the long-term catalog (Fig. 3A) is also observed in the iMUSH catalog (Fig. 2B), though to a lesser extent owing to the lesser event count.

We report the fault-plane solutions for a total of 181 events (Figs. 5, S3, S4, S5. S6), which have a solution quality score of A or B, recorded by the XD and permanent networks from July 2014 to August 2016. SKHASH reports two nodal fault planes as part of the complete fault plane solution (Skoumal et al., 2024). Whether a nodal plane is output as "primary" and "auxiliary" is arbitrary and is examined in the Discussion section. In addition, we compute pressure and tensile (P/T) axes with the Pyrocko moment_tensor module (Heimann et al., 2017). Without augmentation from the XD network, few if any events would have adequate focal sphere coverage to reliably constrain a fault-plane solution. We show all fault-plane solutions in Figure 5 and zoomed-in views of all four seismicity groups in Supplementary Figures S5, S6, S7, and S8.

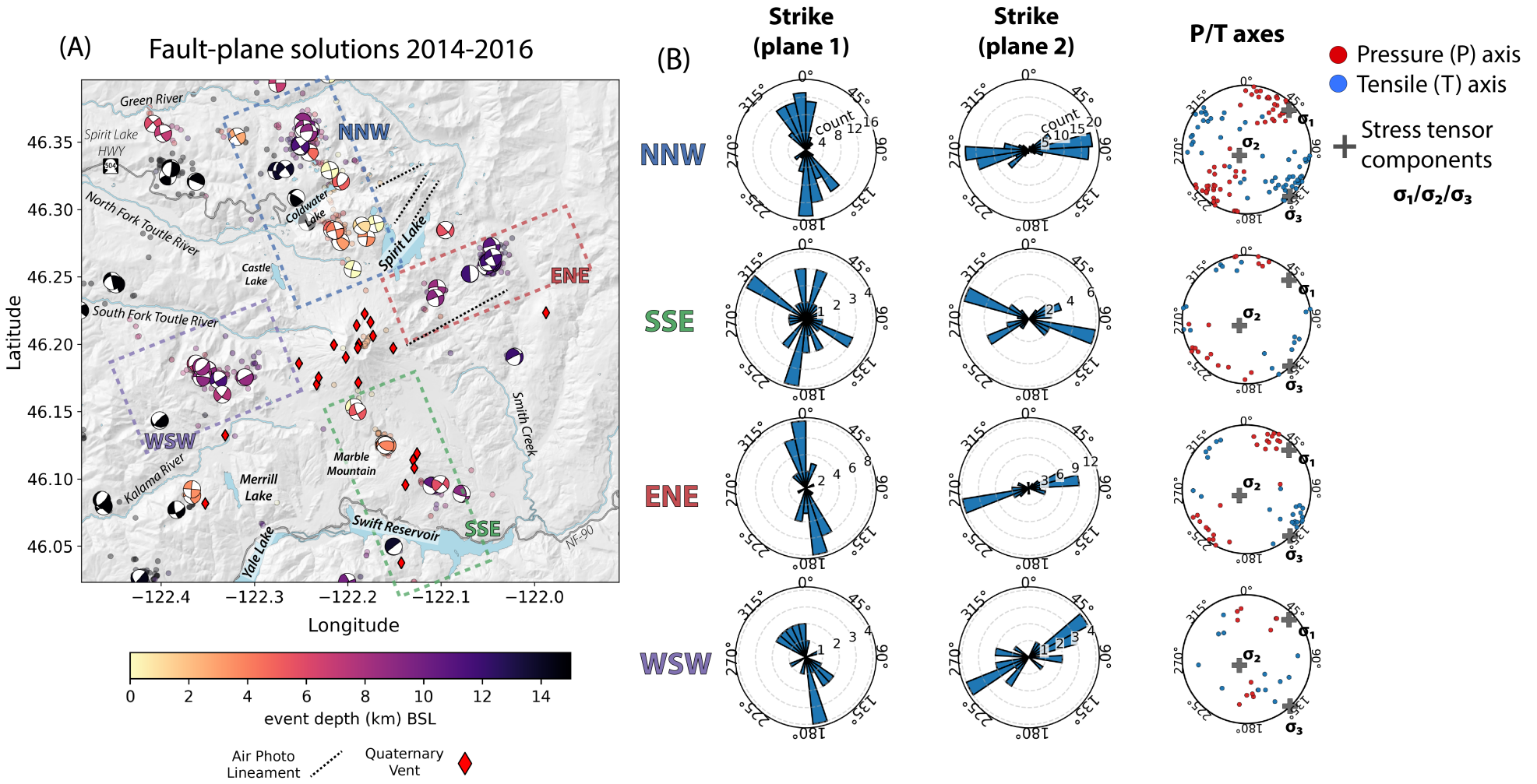


Figure 5 Map (A) of fault-plane solutions using the Imaging Under Mount St. Helens (iMUSH) XD and permanent networks from 2014–2016. The transparent colored dots are locations of events in the iMUSH catalog that do not have a fault-plane solution. Panel (B) shows the strikes of both nodal planes and pressure/tensile (P/T) axes of fault-plane solutions in each of the four seismicity groups. The P/T axes are plotted with the stress tensor solutions of Giampiccolo et al. (1999) σ_1, σ_2 , and σ_3 are the orientations of largest, middle, and smallest compressive principal stress components of the stress tensor from Giampiccolo et al. (1999) Red diamonds are Quaternary vents, such as in Figure 1. See supporting figures S5, S6, S7, and S8 for zoomed-in views.

In the NNW group we observe a total of 59 predominantly NNW–SSE striking, steeply dipping strike-slip FPS along the NNW–SSE trending lineation of seismicity hypocenters (Figs. 5, S5). The distributions of primary fault-plane strike and corresponding pressure and tensile axes indicate low variability among FPS in the NNW group. In addition, the NNW group contains the M_d 4.3 event of February 2011 which is associated with a large non-double couple component and steeply dipping NW-striking nodal plane, described in Section 2.6. The SSE group contains comparatively fewer well-resolved solutions—only 18 in total, which lie along a similar NW–SE striking trend observed in epicenters of both the long-term and iMUSH catalogs. In addition, fault-plane solutions in the SSE group are more heterogeneous than in the NNW group (Fig. 5). Here, we observe only a few FPS which are consistent with strike-slip motion along the southern St. Helens seismic zone, as observed in the NNW group. The remaining solutions generally consist of mechanisms consistent with dip-slip thrust-faulting motion along either NW–SE or SW–NE oriented fault planes.

The WSW group contains 12 well-resolved fault-plane solutions, the fewest of all four seismicity groups (Figs. 5, S7). Fault-plane solutions in the WSW group fall into two categories: (1) FPS consistent with normal dip-slip along steep, ENE–WSW oriented primary planes that orient directly towards and away from Mount St. Helens, and (2) strike-slip along near-vertical NW–SE or NE–SW oriented faults. The ENE group contains a total of 24 well-constrained fault-plane solutions (Fig. S8), most of which are very similar to each other and those observed in the NNW group. These mechanisms are consistent with steeply dipping strike-slip faults along a NNW–SSE or ENE–WSW fault plane. Additionally, the ENE group contains the M_L 3.9 event of January 2018, which reflects dip-slip normal faulting along a NE–SW oriented fault plane, a mechanism which is not like any other fault-plane solution in the ENE group from the 2014–2016 period.

4 Discussion

Our enhanced earthquake catalogs show that most non-volcanic seismicity nearest to Mount St. Helens organizes into four distinct groups that are located near its NNW, SSE, WSW, and ENE flanks (Figs. 2, 3). Seismic activity within all four groups, aside from the SSE group, is persistent throughout most of entire study period. In addition, each of the four groups are separated from VT earthquakes directly beneath Mount St. Helens by approximately equal distances of roughly 5–7 km. While the distinction between separate VT and tectonic earthquakes is often ill-defined, we find clear spatial separation between volcanic earthquakes beneath Mount St. Helens and adjacent faults that is reflected in both the template starting locations (Fig. S1) and final relative locations (Fig. 2).

We examine whether the broad-scale spatial and temporal observations we list here are the result of interaction between the underlying tectonic structure and forces from the volcanic system. To evaluate whether our fault plane solutions can be explained by the regional background stress state, we compare their nodal planes and pressure and tensile axes with the stress tensor of Giampiccolo et al. (1999). Stress tensor orientations around the Mount St. Helens region are typically inferred through the inversion of fault plane solutions (Ma et al., 1991; Giampiccolo et al., 1999), and the orientations show that the maximum compressive stress (σ_1) is nearly horizontal in a NE–SW trend (Fig. 5B), consistent with the Juan de Fuca-North American plate boundary convergence vector of N50E (Fig. 1A). Further evidence of a NE–SW maximum horizontal compressive stress is found in ENE–WSW trending fracture orientations (Fig. 1B), and lineations of volcanic vents (Figs. 1B, 3A, 5A; Evarts et al., 1987).

4.1 Fault architecture near Mount St. Helens: possible orthogonal fracture zones?

The orthogonal configuration of the four non-volcanic seismicity groups around Mount St. Helens (Figs. 2, 3) is striking. The locations may be explained by near-orthogonal fracture zones that intersect beneath Mount St. Helens. If true, the apex of orthogonal fracture zones could form a high-permeability pathway, which may assist the upward migration of magmatic fluids towards the shallow depths, contributing to the formation of the upper-crustal Mount St. Helens volcanic complex. Alternatively, it is possible that all four or some of the non-volcanic seismicity groups simply occur along faults that are not related to the Mount St. Helens magmatic system and are coincidental. Here, we inspect our catalog of focal mechanisms and compare them to mapped geologic features to evaluate the possibility that Mount St. Helens is underlain by intersecting fracture zones.

Double-couple fault-plane solutions yield two orthogonal nodal planes which can equally explain the observed polarity patterns. Due to this inherent non-uniqueness, prior knowledge of the geologic setting is necessary to constrain the most plausible nodal plane. The hypocenter distributions and NNW–SSE to NW–SE oriented nodal planes of focal mechanisms within the NNW and SSE non-volcanic groups are consistent with the geometry of the St. Helens seismic zone revealed by magnetotelluric (Hill et al., 2009; Bedrosian et al., 2018) and velocity imaging (Kiser et al., 2019; Ulberg et al., 2020) studies. The spatial footprint of the NNW group overlaps with the 1981 M5.5 Elk Lake earthquake source region (Fig. 1B). Moreover, strike-slip mechanisms of NNW–SSE and NW–SE orientations in the NNW and SSE groups, respectively, resemble the fault-plane solutions of Weaver et al. (1987), which were used to originally define the St. Helens seismic zone. Pressure axes from events in the NNW group align closely with the NE–SW trend of the σ_1 component of the regional stress tensor from Giampiccolo et al. (1999). The NNW–SSE to NW–SE strike and near vertical dip of the St. Helens seismic zone make it well-oriented for slip, given the NE–SW trending maximum compressive stress (Giampiccolo et al., 1999, Fig. 5B). Slip along the WSW–NE auxiliary plane is less likely given the NNW–SSE trend

of hypocenters.

The WSW and ENE seismicity groups both contain a significant number of fault-plane solutions with candidate nodal planes that reflect a WSW–ENE fracture zone that point towards Mount St. Helens. The WSW group contains focal mechanisms that suggest a combination of slip along NW–SE or NE–SW oriented strike-slip faults and steeply dipping normal faults along WSW–ENE oriented plane (Fig. 5). The orientation of the WSW and ENE groups parallels that of the row of volcanic vents and mapped fractures mapped by Evarts et al. (1987). Here, normal faulting may be favored due to a combination of inherited WSW–ENE trending fractures, lithostatic stresses at 8 to 14 km BSL (roughly 210 to 370 MPa, given rock density of 2700 kg/m^3 and gravitational acceleration of 9.8 m/s^2) and localized rotations in the stress field due to lithologic heterogeneities.

The focal mechanisms in the ENE group between 2014 and 2016 reflect strike-slip along either NNW–SSE or WSW–ENE oriented nodal planes. These mechanisms closely resemble those found in the NNW group and have little variation. Without measurable surface deformation or direct observation of the fault, it is difficult to determine whether slip occurs along either the NNW–SSE plane or the WSW–ENE plane. If the NNW–SSE plane is favorable, it suggests that the ENE group could reflect an offset splay fault of the St. Helens seismic zone or along a series of NNW–SSE trending en echelon faults. On the other hand, the WSW–ENE candidate nodal plane is subparallel to a set of NE–SW air photo lineaments, or pyrite bearing dikes found in the Spirit Lake batholith, east of the St. Helens seismic zone (Fig. 1). In addition, the NE–SW oriented normal faulting event of January 2018 (Fig. 3) provides some further evidence a roughly NE–SW oriented fracture zone that points towards Mount St. Helens may exist in the ENE group. Similar to normal faulting events in the WSW group, we propose that dip-slip normal faulting can occur along an inherited fracture zone parallel to the regional σ_1 promoted by lithostatic stresses at 10 to 14 km BSL and lithologic heterogeneity.

Our analysis of hypocenters and focal mechanisms within both the WSW and ENE non-volcanic groups, and agreement with trends of known geologic structures, provide some evidence for fracture zones oriented suborthogonal to the St. Helens seismic zone. Given the lack of earthquake rate correlation and spatial separation of the four non-volcanic seismicity groups with volcano-tectonic seismicity, it is unclear if these two fractures zones form a continuous structure that intersects the St. Helens seismic zone beneath Mount St. Helens. If we suppose that the NE–SW fracture zone and St. Helens seismic zone do intersect beneath the volcano, we hypothesize that this could form a high-permeability pathway that encourages the upward migration of melt and volatiles from midcrustal depths. We further propose that the spatial separation of volcanic and nonvolcanic seismicity could be attributed to a lateral, thermally modulated brittle-ductile transition surrounding the magmatic reservoir between approximate 5–15 km depth BSL (Fig. 3). In our view, volcano-tectonic seismicity within the Mount St. Helens volcanic complex is different from non-volcanic seismicity examined in this paper. Volcano-tectonic seismicity between 5 to 8 km BSL occurs around a pressurizing magma chamber, above which volcano-tectonic seismicity is hosted within brittle magma primarily by volatile flux (e.g., Moran, 1994; Hirao et al., 2025). Further distinction between volcano-tectonic seismicity and tectonic seismicity at Mount St. Helens may be drawn from differences in their respective stress tensors. Volcano-tectonic seismicity typically yields stress tensors with maximum principal stress axes oriented radially from the volcano (Musumeci et al., 2000). By comparison, stress tensors from tectonic seismicity are consistent with the regional stress tensor, driven by plate convergence at the Juan de Fuca and North American plate boundary (Zoback and Zoback, 1989; Ma et al., 1991; Giampiccolo et al., 1999, Figs. 1A, 5B).

4.2 Fault heterogeneity and fluid circulation along the St. Helens seismic zone

Both northern and southern sections of the St. Helens seismic zone can host earthquakes of moderate magnitude (M > 5; Fig. 1) and persistent low magnitude seismicity (Moran, 1994). Non-volcanic seismicity within the northern section of the St. Helens seismic zone (i.e. the NNW group) differs from seismicity in the southern section (i.e. the SSE group). Seismicity in the northern section is more frequent, contains events of higher recorded magnitudes (M5.5 of 1981; Weaver and Smith, 1983; Weaver et al., 1987), is distributed more continuously (Figs. 2, 3), and features less variation of fault-plane solutions (Fig. 5). By contrast, seismicity in the SSE group is less frequent, more disjointed, and is more heterogeneous in its fault-plane solutions (Figs. 3, 5). More frequent slip cycles along the NNW group could lead to the formation of a more mature, homogeneous, and continuous fault surface (e.g., Guo et al., 2023). In addition, Quaternary vents along the southern St. Helens seismic zone could interfere with a throughgoing fault zone along the SSE group (Figs. 2, 5). Here, thrust mechanisms near and along strike of the Quaternary vents could reflect localized transpression within the St. Helens seismic zone itself, or compression against small-scale volcanic units of higher stiffness (Fig. 5).

Both the NNW and SSE groups show systematic increase in hypocentral depth with distance from the volcano (Figs. 2, 3, S4). Given that the depth change is not observed with the WSW or ENE seismicity groups, we propose that the change in depth away from Mount St. Helens reflects elevated fluid diffusivity along the St. Helens seismic zone. Enhanced diffusivity allows for the permeation of high temperature fluids around the volcano, which in turn heats the fault zone to temperatures at depths below 5 to 8 km beyond a brittle-ductile threshold. Away from the volcano, cooler temperatures that permit brittle failure along the St. Helens seismic zone can be achieved at greater depths. We therefore suggest a higher temperature gradient along the St. Helens seismic zone than in the surrounding bedrock to its east and west.

Several independent observations indicate that the

St. Helens seismic zone hosts hydrothermal fluid circulation. Magnetotelluric and seismic imaging at the regional scale (Hill et al., 2009; Bedrosian et al., 2018; Swyer et al., 2018), in addition to the geothermal surveys at local field scales, indicate that geothermal fluid circulation is present along the St. Helens seismic zone near both the NNW and SSE nonvolcanic groups (Norman et al., 2015; Swyer et al., 2018; Steely et al., 2021). In particular, the NNW seismicity group overlaps or is directly beneath tomographically imaged bodies of high electrical conductivity and high V_p/V_s (greater than 1.9; Swyer et al., 2018). In addition, an elevated geothermal gradient of 50 C°/km is observed in the northern St. Helens seismic zone at a temperature-gradient well along the Green River (Fig. 1, Norman et al., 2015). We suggest that higher levels of fluid circulation along a focused pathway could support higher sustained seismicity rates along the NNW group, compared with the SSE. It is unclear if fluids in the northern and southern St. Helens seismic zone are directly connected to the magmatic reservoir beneath Mount St. Helens (Norman et al., 2015).

4.3 Do the earthquake groups interact?

Seismicity within each of the four non-volcanic groups are spatially separated from each other and from VT events beneath the volcano. Thus, at no point in our study period do earthquakes from any of the four non-volcanic seismicity groups appear to migrate from group to group (Fig. 3B), nor interact with VT events within the Mount St. Helens volcanic plumbing system. In addition, the event rates of each of the four non-volcanic seismicity groups and those of VT earthquakes are uncorrelated. Likewise, we do not observe focal mechanism patterns near the volcano that would indicate magmatic inflation or deflation, such as ring-like dip-slip faulting surrounding the edifice. Thus, the spatial separation of non-volcanic and volcanic seismicity, lack of temporal correlation of event rates, and lack of ring-like faulting around the volcano indicate that direct interaction between volcanic and adjacent tectonic structures during the 2008 to 2024 study period is unlikely or not observable through seismicity alone.

Our earthquake catalogs show a lack of correlation among VT earthquakes within the Mount St. Helens upper-crustal magmatic transport system and non-volcanic earthquakes in the surrounding fault zones within the 2008 to 2024 study period. In addition, there are no known changes in earthquake rate activity of the four nonvolcanic groups prior to or in response to the 2004–2008 eruption. However, the largest known event in this region, the M5.5 Elk Lake earthquake of February 1981, occurred during a period of frequent eruptive activity in the 1980–1986 Mount St. Helens eruptive sequence, roughly 9 months after the Plinian eruption of May 1980 (e.g., Lipman and Mullineaux, 1981). Since February 1981, there is yet to be another recorded earthquake of magnitude 5 or greater. The lack of known recurrence intervals of M5 events along the northern St. Helens seismic zone makes it difficult to infer a relationship between eruptive activity at Mount St. Helens in the 1980s and the 1981 M5.5 earthquake.

4.4 Seismicity and upper crustal structure in southern Washington, USA

Weaver et al. (1987) suggest that the change of strike along the St. Helens seismic zone from NNW–SSE to NW–SE lends itself to crustal extension and the formation of a pull-apart basin-like feature beneath Mount St. Helens. Through our analysis of high-precision earthquake locations, focal mechanisms, and geologic features, we suggest that crustal extension proposed by Weaver et al. (1987) is not required to explain the location of Mount St. Helens relative to the main Cascade Arc volcanoes. Moreover, we do not know of any clear evidence to show that decompression melting alone is a dominant mechanism for melt supply at the volcano. Compared to typical crustal fluids, multiphase melts are substantially higher in viscosity and require larger fracture widths to transfer through Earth's crust. Here, such a fracture zone may develop through intersection of the St. Helens seismic zone and sub-orthogonal faults, which is made evident through patterns of earthquake locations and their focal mechanisms. We therefore suggest that the position and westward offset of Mount St. Helens from the main volcanic arc may be explained by the focusing of melt through the apex of these two fault zones.

The St. Helens seismic zone is one of the most seismically active crustal faults in southern Washington, USA (Grant et al., 1984). In our catalogs, seismicity along the St. Helens seismic zone maps well onto a part of an interconnected regional-scale electrically conductive volume of partial melt, where the ascents of partial melts and volatiles from mid- to lower-crustal origin are focused between the accreted Siletzia pillow basalts and Spirit Lake batholith—both of which are inherited from the development of the Cascade Arc margin, which in turn controls the distribution volcanic vents in the upper plate. We extend the hypothesis of Bedrosian et al. (2018)—here, upper crustal faulting may form along inherited terrane boundaries that meet at optimal angles with respect to the regional stress tensor (e.g., Evarts et al., 1987). Persistent seismicity may be maintained through a constant background stressing rate and upward-migrating volatiles through high permeability channels along the St. Helens seismic zone.

5 Conclusion

Mount St. Helens is underlain by the St. Helens seismic zone, a right-lateral strike-slip fault zone that may channel volatiles from mid-crustal depths between the Siletzia and Spirit Lake batholith terranes. To better characterize the interaction between the active volcanic plumbing system and adjacent tectonic structures, we create two high-resolution enhanced catalogs of non-volcanic seismicity. Here, we construct a long-term catalog spanning from 2008 to 2024 and a short-term catalog that leverages the temporary, high-density configuration of the Imaging Under Mount St. Helens (iMUSH) dense array, spanning from 2014–2016. We

then make further use of the iMUSH catalog to solve for over 180 fault-plane solutions to resolve fault architecture near Mount St. Helens. Our enhanced catalogs show that nonvolcanic seismicity clusters into four distinct groups that lie within 5 to 20 km of the volcano. These groups appear to be temporally uncorrelated with volcano-tectonic activity; we do not find evidence for migration or correlated event rates between groups. Detailed analysis of hypocenters, fault-plane solutions, and mapped geologic features indicate a possible sub-orthogonal fracture zone that intersects at the Mount St. Helens magmatic plumbing system. This feature could assist in the upward migration of magmatic volatiles and melt which form the Mount St. Helens volcanic plumbing complex.

Acknowledgements

The material presented in this manuscript is supported by the U.S. Geological Survey (USGS) Cooperative Agreement G23AC00557 and NSF 1848302. This work was partially completed with a USGS Pathways Internship. The quality of this study benefitted from thoughtful reviews of Margaret Glasgow and two anonymous reviewers and the editorial oversight of Christos Evangelidis. We extend appreciation to Katherine Cashman, Emillie Hooft, and Rachel Abercrombie for thoughtful conversations that contributed to this manuscript. Lastly, we thank Daniel Trugman for help with the GrowClust3D algorithm, Anthony Lomax for help with the NonLinLoc package, the University of Oregon Research Advanced Computing Services staff for their support of the high-performance computing cluster "Talapas", and the staff at the Pacific Northwest Seismic Network for their earthquake catalog. Any use of trade, firm, or product names is for descriptive purposes only and does not imply endorsement by the U.S. Government.

Data and code availability

Files containing the long-term and iMUSH/XD earthquake catalogs and focal mechanisms are uploaded to the Hirao et al. (2026) repository; its headers are described in Supplementary Material Text S1. Waveform data are retrieved from the IRIS Data Management Center (IRIS Data Management Center; Trabant et al., 2012) and are supplied by the UW (University of Washington, 1963), CC (Cascades Volcano Observatory/USGS, 2001), PB (UNAVCO), UO (University of Oregon, 1990), and XD (Creager, 2014) seismic networks. Continuous waveforms and event template data, including phase picks, starting magnitudes, polarities, and station metadata were obtained from the Pacific Northwest Seismic Network (University of Washington, 1963).

Competing interests

The authors have no competing interests.

References

Aki, K. and Richards, P. G. *Quantitative Seismology: Theory and Methods*. W. H. Freeman, San Francisco, 1980.

Altamimi, Z., Métivier, L., Rebischung, P., Collilieux, X., Chanard, K., and Barnéoud, J. ITRF2020 plate motion model. *Geophysical Research Letters*, 50(24):e2023GL106373, 2023. doi: 10.1029/2023GL106373.

Bedrosian, P. A., Peacock, J. R., Bowles-Martinez, E., Schultz, A., and Hill, G. J. Crustal inheritance and a top-down control on arc magmatism at Mount St Helens. *Nature Geoscience*, 11(11): 865–870, 2018. doi: 10.1038/s41561-018-0217-2.

Beyreuther, M., Barsch, R., Krischer, L., Megies, T., Behr, Y., and Wassermann, J. ObsPy: A Python Toolbox for Seismology. *Seismological Research Letters*, 81(3):530–533, 2010. doi: 10.1785/gssrl.81.3.530.

Cascades Volcano Observatory/USGS. Cascade Chain Volcano Monitoring, 2001. doi: 10.7914/SN/CC. Data set.

Creager, K. Collaborative Research: Illuminating the architecture of the greater Mount St. Helens magmatic systems from slab to surface, 2014. doi: 10.7914/SN/XD_2014. Data set.

Dziewonski, A. M., Chou, T.-A., and Woodhouse, J. H. Determination of earthquake source parameters from waveform data for studies of global and regional seismicity. *Journal of Geophysical Research*, 86:2825–2852, 1981. doi: 10.1029/JB086iB04p02825.

Dzurisin, D. Mount St. Helens Retrospective: Lessons Learned Since 1980 and Remaining Challenges. *Frontiers in Earth Science*, 6:142, 2018. doi: 10.3389/feart.2018.00142.

Dzurisin, D., Moran, S. C., Lisowski, M., Schilling, S. P., Anderson, K. R., and Werner, C. The 2004–2008 dome-building eruption at Mount St. Helens, Washington: Epilogue. *Bulletin of Volcanology*, 77(10):89, 2015. doi: 10.1007/s00445-015-0973-4.

Ekström, G., Nettles, M., and Dziewoński, A. M. The global CMT project 2004–2010: Centroid-moment tensors for 13,017 earthquakes. *Physics of the Earth and Planetary Interiors*, 200–201: 1–9, 2012. doi: 10.1016/j.pepi.2012.04.002.

Evarts, R. C., Ashley, R. P., and Smith, J. G. Geology of the Mount St. Helens area: Record of discontinuous volcanic and plutonic activity in the Cascade Arc of southern Washington. *Journal of Geophysical Research: Solid Earth*, 92(B10):10155–10169, 1987. doi: 10.1029/JB092iB10p10155.

Finn, C. and Williams, D. L. An aeromagnetic study of Mount St. Helens. *Journal of Geophysical Research: Solid Earth*, 92(B10): 10194–10206, 1987. doi: 10.1029/JB092iB10p10194.

Giampiccolo, E., Musumeci, C., Malone, S. D., Gresta, S., and Privitera, E. Seismicity and stress-tensor inversion in the central Washington Cascade Mountains. *Bulletin of the Seismological Society of America*, 89(3):811–821, 1999. doi: 10.1785/BSSA0890030811.

Grant, W. C., Weaver, C. S., and Zollweg, J. E. The 14 February 1981 Elk Lake, Washington, earthquake sequence. *Bulletin of the Seismological Society of America*, 74(4):1289–1309, 1984. doi: 10.1785/BSSA0740041289.

Guo, H., Lay, T., and Brodsky, E. E. Seismological Indicators of Geologically Inferred Fault Maturity. *Journal of Geophysical Research: Solid Earth*, 128(10):e2023JB027096, 2023. doi: 10.1029/2023JB027096.

Han, J., Vidale, J. E., Houston, H., Schmidt, D. A., and Creager, K. C. Deep Long-Period Earthquakes Beneath Mount St. Helens: Their Relationship to Tidal Stress, Episodic Tremor and Slip, and Regular Earthquakes. *Geophysical Research Letters*, 45 (5):2241–2247, 2018. doi: 10.1002/2018GL077063.

Hansen, S. M., Schmandt, B., Levander, A., Kiser, E., Vidale, J. E.,

Abers, G. A., and Creager, K. C. Seismic evidence for a cold serpentinized mantle wedge beneath Mount St Helens. *Nature Communications*, 7:13242, 2016. doi: 10.1038/ncomms13242.

Hardebeck, J. L. and Shearer, P. M. A new method for determining first-motion focal mechanisms. *Bulletin of the Seismological Society of America*, 92(6):2264–2276, 2002. doi: 10.1785/0120010200.

Heimann, S., Kriegerowski, M., Isken, M. P., Cesca, S., Daout, S., Grigoli, F., Juretzek, C., Megies, T., Nooshiri, N., Steinberg, A., Sudhaus, H., Vasyura-Bathke, H., Willey, T., and Dahm, T. Pyrocko: An open-source seismology toolbox and library, 2017. doi: 10.5880/GFZ.2.1.2017.001. Computer software.

Hildreth, W. Quaternary magmatism in the Cascades — Geologic perspectives. U.S. Geological Survey Professional Paper 1744, U.S. Geological Survey, 2007. doi: 10.3133/pp1744.

Hill, G. J., Caldwell, T. G., Heise, W., Chertkoff, D. G., Bibby, H. M., Burgess, M. K., Cull, J. P., and Cas, R. A. F. Distribution of melt beneath Mount St Helens and Mount Adams inferred from magnetotelluric data. *Nature Geoscience*, 2:785–789, 2009. doi: 10.1038/ngeo661.

Hirao, B., Thomas, A., Thelen, W., Shelly, D., Journeau, C., and Iezzi, A. Dataset for "Seismotectonics of the Mount St. Helens Region", 2026. doi: 10.5281/zenodo.18916956. Data set.

Hirao, B. W., Thomas, A. M., Shelly, D. R., Thelen, W. A., and Journeau, C. Magmatic Volatile Flux Drives Non-Eruptive Volcano-Tectonic Seismicity at Mount St. Helens, USA From 2008–2024. *Journal of Geophysical Research: Solid Earth*, 130 (12):e2025JB031278, 2025. doi: 10.1029/2025JB031278.

Hutton, L. K. and Boore, D. M. The M_L scale in southern California. *Bulletin of the Seismological Society of America*, 77(6): 2074–2094, 1987. doi: 10.1785/BSSA0770062074.

Kiser, E., Palomeras, I., Levander, A., Zelt, C., Harder, S., Schmandt, B., Hansen, S., Creager, K., and Ulberg, C. Magma reservoirs from the upper crust to the Moho inferred from high-resolution Vp and Vs models beneath Mount St. Helens, Washington State, USA. *Geology*, 44(6):411–414, 2016. doi: 10.1130/G37591.1.

Kiser, E., Levander, A., Zelt, C., Schmandt, B., and Hansen, S. Upper Crustal Structure and Magmatism in Southwest Washington: V_p, V_s, and V_p/V_s Results From the iMUSH Active-Source Seismic Experiment. *Journal of Geophysical Research: Solid Earth*, 124(7):7067–7080, 2019. doi: 10.1029/2018JB016203.

Lipman, P. W. and Mullineaux, D. R., editors. *The 1980 eruptions of Mount St. Helens, Washington*. Number 1250 in U.S. Geological Survey Professional Paper. U.S. Geological Survey, 1981. doi: 10.3133/pp1250.

Lomax, A., Zollo, A., Capuano, P., and Virieux, J. Precise, absolute earthquake location under Somma-Vesuvius volcano using a new three-dimensional velocity model. *Geophysical Journal International*, 146(2):313–331, 2001. doi: 10.1046/j.0956-540x.2001.01444.x.

Lomax, A., Michelini, A., and Curtis, A. Earthquake location, direct, global-search methods. In Meyers, R. A., editor, *Encyclopedia of complexity and systems science*, pages 2449–2473. Springer, 2009. doi: 10.1007/978-0-387-30440-3_150.

Ma, L., Crosson, R. S., and Ludwin, R. S. Focal mechanisms of western Washington earthquakes and their relationship to regional tectonic stress. Open-File Report 91-441-D, U.S. Geological Survey, 1991. doi: 10.3133/ofr91441D.

Moran, S. C. Seismicity at Mount St. Helens, 1987–1992: Evidence for repressurization of an active magmatic system. *Journal of Geophysical Research*, 99(B3):4341–4354, 1994. doi: 10.1029/93JB02993.

Mousavi, S. M., Sheng, Y., Zhu, W., and Beroza, G. C. STanford EArthquake Dataset (STEAD): A global data set of seismic signals for AI. *IEEE Access*, 7:179464–179476, 2019. doi: 10.1109/ACCESS.2019.2947848.

Musumeci, C., Malone, S. D., Giampiccolo, E., and Gresta, S. Stress tensor computations at Mount St. Helens (1995–1998). *Annals of Geophysics*, 43(5):889–904, 2000. doi: 10.4401/ag-3681.

Nichols, M. L., Malone, S. D., Moran, S. C., Thelen, W. A., and Vidale, J. E. Deep long-period earthquakes beneath Washington and Oregon volcanoes. *Journal of Volcanology and Geothermal Research*, 200(3–4):116–128, 2011. doi: 10.1016/j.jvolgeores.2010.12.005.

Norman, D. K., Forson, C., Czajkowski, J. L., Swyer, M. W., Cladouhos, T. T., Schmalzle, G. M., and Davatzes, N. C. Geothermal play-fairway analysis of Washington State prospects: Phase 1 technical report. Technical Report DE-EE0006728, Washington Division of Geology and Earth Resources, 2015. doi: 10.15121/1261949.

O'Hara, D., Karlstrom, L., and Ramsey, D. W. Time-evolving surface and subsurface signatures of Quaternary volcanism in the Cascades arc. *Geology*, 48(11):1088–1093, 2020. doi: 10.1130/G47706.1.

Pedregosa, F., Varoquaux, G., Gramfort, A., Michel, V., Thirion, B., Grisel, O., Blondel, M., Prettenhofer, P., Weiss, R., Dubourg, V., Vanderplas, J., Passos, A., Cournapeau, D., Brucher, M., Perrot, M., and Duchesnay, E. Scikit-learn: Machine learning in Python. *Journal of Machine Learning Research*, 12:2825–2830, 2011. https://www.jmlr.org/papers/v12/pedregosa11a.html.

Qamar, A. I., Rathbun, A., Ludwin, R. S., Noson, L. L., Crosson, R. S., and Malone, S. D. Earthquake hypocenters in Washington and northern Oregon—1981. Information Circular 83, Washington State Department of Natural Resources, Division of Geology and Earth Resources, 1987. https://dnr.wa.gov/Publications/ger_ic83_eq_hypocenters_western_wa_1981.pdf.

Richter, C. F. An instrumental earthquake magnitude scale. *Bulletin of the Seismological Society of America*, 25(1):1–32, 1935. doi: 10.1785/BSSA0250010001.

Ronneberger, O., Fischer, P., and Brox, T. U-Net: Convolutional networks for biomedical image segmentation. In Navab, N., Hornegger, J., Wells, W. M., and Frangi, A. F., editors, *Medical image computing and computer-assisted intervention—MICCAI 2015*, volume 9351 of *Lecture Notes in Computer Science*, pages 234–241. Springer, 2015. doi: 10.1007/978-3-319-24574-4_28.

Senobari, N. S., Funning, G. J., Keogh, E., Zhu, Y., Yeh, C.-C. M., Zimmerman, Z., and Mueen, A. Super-Efficient Cross-Correlation (SEC-C): A fast matched-filtering code suitable for desktop computers. *Seismological Research Letters*, 2018. doi: 10.1785/0220180122.

Shelly, D. R., Ellsworth, W. L., and Hill, D. P. Fluid-faulting evolution in high definition: Connecting fault structure and frequency-magnitude variations during the 2014 Long Valley Caldera, California, earthquake swarm. *Journal of Geophysical Research: Solid Earth*, 121(3):1776–1795, 2016. doi: 10.1002/2015JB012719.

Skoumal, R. J., Hardebeck, J. L., and Shearer, P. M. SKHASH: A Python Package for Computing Earthquake Focal Mechanisms. *Seismological Research Letters*, 95(4):2519–2526, 2024. doi: 10.1785/0220230329.

Steely, A., Cladouhos, T., Davatzes, N., Allen, C., Swyer, M., Spake, D., Stowe, B., Anderson, M., Ritzinger, B., Peacock, J., DeAngelo, J., Schermerhorn, W., Crosbie, K., Ulberg, C., Schmalzle, G., Garrison, G., Norman, D., Glen, J., Czajkowski, J., et al. Geothermal Play-Fairway Analysis of Washington State Prospects: Final Report. Technical Report DOE-WGS-6728, Washington Geological

Survey, 2021. doi: 10.2172/1823116. Author list abbreviated in source.

Swyer, M. W., Uddenberg, M. E., Cladouhos, T. T., Steely, A. N., Forson, C., and Davatzes, N. C. Preliminary geothermal resource assessment of the St. Helens Seismic Zone using the results from the geothermal play-fairway analysis of Washington State prospects. In *Proceedings of the 43rd Workshop on Geothermal Reservoir Engineering*, number SGP-TR-213. Stanford University, 2018. https://pangea.stanford.edu/ERE/pdf/IGAstandard/SGW/2018/Swyer.pdf.

Trabant, C., Hutko, A. R., Bahavar, M., Karstens, R., Ahern, T., and Aster, R. Data Products at the IRIS DMC: Stepping Stones for Research and Other Applications. *Seismological Research Letters*, 83(5):846–854, 2012. doi: 10.1785/0220120032.

Trugman, D. T., Chamberlain, C. J., Savvaidis, A., and Lomax, A. GrowClust3D.jl: A Julia Package for the Relative Relocation of Earthquake Hypocenters Using 3D Velocity Models. *Seismological Research Letters*, 94(1):443–456, 2023. doi: 10.1785/0220220193.

Ulberg, C. W., Creager, K. C., Moran, S. C., Abers, G. A., Thelen, W. A., Levander, A., Kiser, E., Schmandt, B., Hansen, S. M., and Crosson, R. S. Local Source V_p and V_s Tomography in the Mount St. Helens Region With the iMUSH Broadband Array. *Geochemistry, Geophysics, Geosystems*, 21(3):e2019GC008888, 2020. doi: 10.1029/2019GC008888.

UNAVCO. Plate Boundary Observatory Borehole Seismic Network (PB). https://www.fdsn.org/networks/detail/PB/. Data set; date not provided.

University of Oregon. Pacific Northwest Seismic Network - University of Oregon, 1990. doi: 10.7914/SN/UO. Data set.

University of Washington. Pacific Northwest Seismic Network - University of Washington, 1963. doi: 10.7914/SN/UW. Data set.

Utsu, T. Representation and analysis of the earthquake size distribution: A historical review and some new approaches. *Pure and Applied Geophysics*, 155(2–4):509–535, 1999. doi: 10.1007/s000240050276.

Vavryčuk, V. Moment Tensors: Decomposition and Visualization. In Beer, M., Kougioumtzoglou, I. A., Patelli, E., and Au, I. S.-K., editors, *Encyclopedia of Earthquake Engineering*, pages 1–16. Springer Berlin Heidelberg, 2015. doi: 10.1007/978-3-642-36197-5_288-1.

Waite, G. P. and Moran, S. C. V_P Structure of Mount St. Helens, Washington, USA, imaged with local earthquake tomography. *Journal of Volcanology and Geothermal Research*, 182(1–2): 113–122, 2009. doi: 10.1016/j.jvolgeores.2009.02.009.

Weaver, C. S. and Smith, S. W. Regional tectonic and earthquake hazard implications of a crustal fault zone in southwestern Washington. *Journal of Geophysical Research: Solid Earth*, 88(B12):10371–10383, 1983. doi: 10.1029/JB088iB12p10371.

Weaver, C. S., Grant, W. C., and Shemeta, J. E. Local crustal extension at Mount St. Helens, Washington. *Journal of Geophysical Research: Solid Earth*, 92(B10):10170–10178, 1987. doi: 10.1029/JB092iB10p10170.

Wiemer, S. and Wyss, M. Minimum magnitude of completeness in earthquake catalogs: Examples from Alaska, the western United States, and Japan. *Bulletin of the Seismological Society of America*, 90(4):859–869, 2000. doi: 10.1785/0119990114.

Woollam, J., Münchmeyer, J., Tilmann, F., Rietbrock, A., Lange, D., Bornstein, T., Diehl, T., Giunchi, C., Haslinger, F., Jozinović, D., Michelini, A., Saul, J., and Soto, H. SeisBench—A Toolbox for Machine Learning in Seismology. *Seismological Research Letters*, 93(3):1695–1709, 2022. doi: 10.1785/0220210324.

Zhang, H., Glasgow, M., Schmandt, B., Thelen, W. A., Moran, S. C., and Thomas, A. M. Revisiting the depth distribution of seismicity before and after the 2004–2008 eruption of Mount St. Helens. *Journal of Volcanology and Geothermal Research*, 430:107629, 2022. doi: 10.1016/j.jvolgeores.2022.107629.

Zhu, W. and Beroza, G. C. PhaseNet: A deep-neural-network-based seismic arrival-time picking method. *Geophysical Journal International*, 216(1):261–273, 2019. doi: 10.1093/gji/ggy423.

Zoback, M. L. and Zoback, M. D. Chapter 24: Tectonic stress field of the continental United States. In *Geological Society of America Memoirs*, volume 172, pages 523–540. Geological Society of America, 1989. doi: 10.1130/MEM172-p523.

The article *Seismotectonics of the Mount St. Helens Region* © 2026 by Brenton W. Hirao is licensed under CC BY 4.0.